ORNL/Sub/90-SF521/02

INTERIM REPORT

INVESTIGATION OF MOISTURE-INDUCED EMBRITTLEMENT OF IRON ALUMINIDES

April 19, 1994

Research sponsored by the U.S. Department of Energy,
Fossil Energy
Advanced Research and Technology Development Materials Program

Report Prepared by
A. Castagna and N.S. Stoloff
Rensselaer Polytechnic Institute
Materials Engineering Department
Troy, NY 12180-3590
under
Subcontract No. 19X-SF521C

for

OAK RIDGE NATIONAL LABORATORY
Oak Ridge, Tennessee 37831
managed by
MARTIN MARIETTA ENERGY SYSTEMS, INC.
for the
U.S. Department of Energy
under Contract No. DE-AC05-84OR21400

DISTRIBUTION OF THIS DOCUMENT IS UNLIMITED

This report has been reproduced directly from the best available copy.

Available to DOE and DOE contractors from the Office of Scientific and Technical Information, P.O. Box 62, Oak Ridge, TN 37831; prices available from (615) 576-8401, FTS 626-8401.

Available to the public from the National Technical Information Service, U.S. Department of Commerce, 5285 Port Royal Rd., Springfield, VA 22161

This report was prepared as a account of work sponsored by an agency of the United States Government. Neither the united States Government nor any agency thereof, nor any of their employees, makes any warranty, expressed or implied, or assumes any legal liability or responsibility of the accuracy, completeness, or usefulness of any information, apparatus, product, or process disclosed, or represents that its use would not infringe privately owned rights. Reference herein to any specific commercial product, process or service by trade name, trademark, manufacturer, or otherwise, does not necessarily constitute or imply its endorsement, recommendation, or favoring by the United States Government or any agency thereof. The views and opinions of authors expresses herein do not necessarily state or reflect those of the United States Government or any agency thereof.

ORNL/Sub/90-SF521/02

INTERIM REPORT

ENVIRONMENTAL EMBRITTLEMENT IN IRON-ALUMINUM ALLOYS

April 19, 1994

Report Prepared by
A. Castagna and N.S. Stoloff
Rensselaer Polytechnic Institute
Materials Engineering Department
Troy, NY 12180-3590
under
Subcontract No. 19X-SF521C

for

OAK RIDGE NATIONAL LABORATORY
Oak Ridge, Tennessee 37831
managed by
MARTIN MARIETTA ENERGY SYSTEMS, INC.
for the
U.S. Department of Energy
under Contract No. DE-AC05-84OR21400

MASTER

DISTRIBUTION OF THIS DOCUMENT IS UNLIMITED

Research sponsored by the U.S. Department of Energy, Fossil Energy Advanced Research and Technology Development Materials Program, DOE/FE AA 15 10 10 0, Work Breakdown Structure Element RPI-2

Introduction

The purpose of this research is to examine the effects of environmental embrittlement on the mechanical properties of an Fe_3Al base intermetallic compound and a disordered iron aluminum alloy. In particular, fatigue crack growth resistance and tensile behavior will be examined. This research is sponsored by the Department of Energy's Fossil Fuel Program and Oak Ridge National Laboratory (ORNL) as part of an effort to develop iron-aluminum intermetallics for use in engineering applications where their corrosion resistance, strength at temperatures up to ≈500°C, and low cost can be utilized.

Binary iron aluminides do not possess high room temperature ductility in air, typically 4-8% [1,2]. Like many other intermetallics and steels, iron aluminides have been shown to be embrittled by gaseous hydrogen and water vapor, which lowers the room temperature ductility even further. Research conducted at Oak Ridge has shown that the predominant embrittling mechanism in Fe_3Al involves a chemical reaction with water vapor in the air and aluminum at the surface of the material [3] according to the following reaction:

$$2Al + 3H_2O \rightarrow Al_2O_3 + 6H$$

This reaction releases monatomic hydrogen at the surface of the material and is shown in this work to be a potent mechanism of embrittlement.

The brittle intermetallics are generally more difficult to work with than more ductile materials, and pose problems in fabricability, resistance to overloads, and early damage detection. However, this intermetallic has demonstrated ductility above 12% - 16% when tested in vacuum or gaseous oxygen environments [1-3]. This result indicates that Fe_3Al is an inherently ductile material and an environmental interaction causes the low ductility in air.

Fe_3Al has been shown to deform by [110] <111> slip which provides for at least 5 slip systems, exhibits only moderate yield and tensile strength, and fractures in a generally transgranular manner [4], all but the last of which are properties associated with inherently ductile materials. With the ductile nature of iron aluminides in mind, many researchers have investigated the mechanisms of embrittlement in iron aluminides [3,5,6] as well as methods of preventing embrittlement such as alloying or coating [7].

Experimental Procedure and Results

Alloy Composition and Heat Treatment

Alloy FA-129 is an ordered Fe_3Al type intermetallic that can exist in the B2 or DO_3 ordered state, depending on the annealing parameters used. Alloy FAP-Y is a disordered alloy. The compositions of FA-129 and FAP-Y are shown in Table I. Both alloys are fabricated at the Oak Ridge National Laboratory (ORNL) by vacuum induction melting, extrusion to a 2.54 cm thickness, and either hot or warm rolling to the final thickness. The initial plate thickness of FA-129 used in compact tension specimens was 5.08 mm, while the initial plate thickness for FA-129 used in tensile tests was 0.76 mm. All FAP-Y material was received in the form of 5.08 mm thick plate.

The annealing parameters for B2 ordered FA-129 consisted of a 700°C anneal for 1 hour with a mineral oil quench, which was then repeated. The annealing parameters for DO_3 ordered FA-129 were the same as for the B2 order heat treatment, with an additional reheat to 500°C for four days with a furnace cool. FAP-Y was annealed twice at 800°C for one hour with a furnace cool.

Table I - Composition and Conditions of Fe-Al Alloys

Alloy	Condition	Fe	Al	Cr	a % Mo	Nb	Zr	C	Y	grain size (μm)
FA-129	wrought	66.17	28.08	5.04	—	0.51	—	0.20	—	*
FAP-Y	wrought	77.07	16.12	5.44	1.07	—	0.11	0.13	0.06	42

* partially recrystallized

Metallography

Metallography was performed on all materials to examine the grain structure. Samples from each plate of FA-129 and FAP-Y were cut on a cut-off wheel from the short transverse, long transverse, and longitudinal directions. These were mounted in either a bake-lite or epoxy mold. Polishing was performed on water lubricated polishing wheels with 240, 400, and 600 grit paper, followed by a cloth covered wheel impregnated with 16 and 9 μm diamond paste, and finally with a felt covered wheel coated with a 0.3 μm alumina slurry. The metallographic specimens were etched in glyceregia (30 ml glycerin, 30 ml HCl, 10 ml HNO_3) until the grain structure became visible. They were then

photographed on a non-polarized metallograph. Polaroid no. 55 film was used in all metallography photographs.

The annealing parameters for FA-129 resulted in a partially recrystallized structure, which was found by researchers at ORNL to provide for the best ductility in the material. Fig. 1(a) shows the grain structure of as received FA-129. Figs 1(b) and 1(c) show the longitudinal direction of B2 and DO_3 ordered FA-129 respectively, after annealing. Large precipitates (up to 5 μm) were seen throughout the FA-129 material. They were scattered in non-homogeneous clusters and tended to segregate at grain boundaries as seen in Fig. 1(d). A variation of the B2 heat treatment also was attempted, in which the first anneal was done at 900°C, and the second at 700°C. Both were one hour anneals followed by a mineral oil quench. The 900°C anneal resulted in a nearly recrystallized material as seen in Fig. 2.

The annealing parameters for FAP-Y resulted in a recrystallized structure with a grain size of 42 μm. Fig. 3(a) shows the grain structure of as-received FAP-Y, and Fig. 3(b) shows the grain structure of FAP-Y after annealing.

Hardness

The micro hardness of alloy FA-129 was measured in the DO_3 and B2 ordered state for each of the plate orientations. Specimens were mounted and polished as described above before being tested. The hardness values on the Rockwell A scale are listed in Table II. No significant variation in hardness was found with either order or orientation.

Vickers hot hardness measurements were performed as well on alloy FA-129. This work was done at the Los Alamos National Laboratory, and the results are shown in Fig. 4. The hardness is seen to drop quickly as temperatures exceed the critical ordering temperature of approximately 550°C.

Table II

Alloy	Order	Rolling Direction	Hardness Rockwell A
FA-129	B2	ST	58.5
FA1-29	B2	LT	58.7
FA-129	B2	Long. Top	58.4
FA-129	DO_3	ST	59.6
FA-129	DO_3	LT	59.6
FA-129	DO_3	Long. Top	59.6

Fatigue Crack Growth

Fatigue crack growth tests were performed on alloy FA-129 in both the B2 and DO_3 ordered states, and on alloy FAP-Y. At room temperature, tests were conducted in hydrogen gas, laboratory air, and oxygen. Elevated temperature fatigue crack growth tests were conducted on FA-129 in air at 150°C in the B2 and DO_3 ordered state, and at 300°C and 450°C in the DO_3 ordered state. Note that the B2 ordered FA-129 was not tested at temperatures above 150°C because an instability in the B2 state at temperatures above 150°C and below 550°C was expected. Fatigue crack growth testing was attempted on B2 ordered FA-129 at 600°C. However, difficulty was encountered with oxidation of the voltage and current leads at this temperature

Compact tension specimens were used in all fatigue tests and were cut by wire Electro-Discharge Machining such that the crack propagation direction would be perpendicular to the rolling direction. Fig. 5 shows the specimen geometry and rolling direction. Prior to testing all specimens were polished to a 0.3μm finish and ultra-sonically cleansed in an acetone bath.

Crack length was monitored via the d.c. potential drop method. Fig. 6 shows the test set-up. A 10 amp current was supplied from a Hewlett Packard power supply via two current leads positioned on either side of the machine notch at a distance of 12.70 mm. The current was monitored via a resistive shunt, which led into an IBM PC computer fitted with a Metrabyte 12 bit analog to digital converter. The potential across the unbroken ligament was measured using with voltage probes on the compact tension specimen located on either side of the machined notch at a distance of 5.08 mm. These probes also led to the analog to

digital converter. In room temperature tests on alloy FA-129, the current leads and voltage probes were attached to the CT specimen using 2/72 sized machine screws bolted into holes which were drilled and tapped into the front face. However, this technique was not suitable for higher temperatures and in all other tests these connections were made by brazing the leads into short holes drilled into the front face.

Temperature was monitored at the specimen surface to correct for bulk resistivity changes using a chromel-alumel thermocouple cemented to the CT specimen as shown in Fig. 6. The thermocouple output was converted into a voltage proportional to the temperature by an Omega thermocouple reader, and this voltage fed into the analog to digital converter. Calibration tests were performed to determine the appropriate temperature vs. resistance curve for each alloy.

Calibration curves were created relating crack length to potential drop by optically measuring the crack length with a calibrated traveling microscope. This system was able to resolve changes in crack length of 50μm. This precision was limited by the optical crack measurements used in the calibration curves.

The load frame used was an MTS servo-hydraulic machine with a 22205 N load cell. All tests were run in load control using a sawtooth waveform at 20Hz, and an R ratio ($\sigma_{min}/\sigma_{max}$) of 0.5.

Software written for a PC allowed a fully automated test procedure. The PC received the load applied to the specimen, current, voltage, and temperature via the analog to digital converter. The PC recorded these data, calculated the crack length, crack growth rate (da/dN) and stress intensity range (ΔK). The appropriate loading waveform was then calculated based on these measurements and the initially specified test parameters. The digital load waveform was then converted to analog form and sent to the MTS as a load-control input for the hydraulic actuators.

When testing in oxygen or hydrogen gas, the environmental chamber was first evacuated to $< 1.3 \times 10^{-4}$ Pa using a diffusion pump fitted with a liquid nitrogen cold trap. The appropriate gas was then admitted to the chamber at a pressure of 2300 Pa (1/3 psi) over atmospheric pressure.

All parameters of the fatigue crack growth tests followed the ASTM E-647 procedures with the exception of the CT specimen size, which was slightly undersized due to constraints in material availability. The fatigue crack growth test was broken down into the following 5 stages:

1) Precracking of the CT specimens was accomplished by fatiguing in 20000 cycle increments at stress intensity levels increasing by 0.5 MPa$\sqrt{m}$ until crack initiation was observed.

2) A ΔK-increasing procedure was implemented at this point. The crack was grown to approximately 0.5 mm before collecting data to be used in the da/dN curves.

3) The ΔK-increasing procedure was continued until either the crack had propagated to 1.0 mm or a da/dN value of 1×10^{-8} m/cycle was achieved.

4) At this point a load shedding procedure was used to reduce the da/dN values back down to approximately 1×10^{-9} m/cycle to measure crack growth rates in the threshold region. This was the lowest growth rate that could be accurately and conveniently measured.

5) The ΔK-increasing routine was then continued until failure. In all stages the R-ratio was held at 0.5 and crack lengths recorded at intervals of 0.1 mm.

The da/dN curves generated at room temperature for FA-129 and FAP-Y in hydrogen gas, air, and oxygen gas are shown in Fig. 7. Note that no curve was generated for alloy FAP-Y in hydrogen gas because stable crack growth could not be achieved.

The da/dN curves generated for B2 ordered FA-129 in air at various temperatures are shown in Fig. 8, and for DO_3 ordered FA-129 in Fig. 9. Note that an experimental error was made originally in the instrumentation of these tests which resulted in an offset of the curves along the ΔK axis. This error was corrected for and Figs. 8 and 9 represent the corrected data.

The threshold and critical stress intensities, and the slope m of the Paris equation { $da/dN = C(\Delta K)^m$ } are tabulated in Table II. The appearances of the corresponding fracture surfaces also are listed, and will be discussed in more detail in the section Fractography of FCG Specimens.

Table II shows that hydrogen gas produces the highest crack growth rates in all cases, while oxygen produces the lowest rates. In addition, crack growth rates in alloy FAP-Y are higher than those in DO_3 ordered FA-129 which are, in turn, higher than those in B2 ordered FA-129. The difference in critical stress intensity in alloy FAP-Y between air and oxygen (8.5%) was much smaller than in B2 (16%) or DO_3 (21%) ordered FA-129, indicating that FAP-Y is less susceptible to moisture-induced embrittlement.

Table III shows that the average value of m (slope of the da/dN curve) increases rapidly as the environment changes from oxygen to air to hydrogen gas at 25°C, with the greater change for DO_3 ordered FA-129 (3.0 in O_2 to 8.8 in H_2 for B2 and 8.5 in O_2 to 25.1 in H_2 for DO_3). The values of m are also consistently higher in FAP-Y than in DO_3 ordered FA-129, and the values of m for DO_3 ordered FA-129 are consistently higher than in B2 ordered FA-129. As with the change in critical stress intensity, the difference in slope m between air and oxygen in alloy FAP-Y is less than the difference measured between air and oxygen for B2 and DO_3 ordered FA-129.

Table II Fatigue Crack Growth Data for FA-129

Alloy	Environ-ment	Fracture Surface	m	ΔK_{TH} (MPa√m)	ΔK_C (MPa√m)
FA-129 (B2)	O_2, 25°C	Dimpled, few striations	3.0	20.0	35.9
FA-129 (B2)	Air, 25°C	TG, many striation	6.9	14.5	29.9
FA-129 (B2)	H_2, 25°C	TG, few striations	8.8	13.8	25.9
FA-129 (DO_3)	O_2, 25°C	Dimpled + cleavage	8.5	13.5	25.1
FA-129 (DO_3)	Air, 25°C	Cleavage + IG	11.2	13.3	19.8
FA-129 (DO_3)	H_2, 25°C	Cleavage + IG	25.1	11.1	17.4
FA-129 (B2)	Air, 150°	Dimpled	4.1	20.4	40.5
FA-129 (DO_3)	Air, 150°C	TG	5.8	18.5	34.5
FA-129 (DO_3)	Air, 300°C	TG	6.5	18.0	33.1
FA-129 (DO_3)	Air, 450°C	TG	8.9	16.2	31.1
FAP-Y	O_2, 25°C	TG	19.7	9.9	12.8
FAP-Y	Air, 25°C	TG	22.2	10.0	11.7
FAP-Y	H_2, 25°C	—	—	—	—

Calculations of the plastic zone size induced in the CT specimens during fatiguing indicate that plane strain conditions may not be satisfied in specimens with high toughness (i.e., B2 ordered FA-129 in O_2 at 25°C, or in air at 150°C). Micro hardness measurements were made on CT specimens fatigued to failure to determine if a large plastic zone occurred. These measurements were made along the edge of the crack front, beginning from the machined notch and continuing past the point of unstable crack growth (start of catastrophic failure). Only a slight increase in hardness was found along the crack in the stable region, while significant hardening was found beyond the point of unstable crack growth. This observation indicates that little work-hardening occurs during fatiguing, and is consistent with predominantly plane strain deformation.

Another concern in the fatigue crack growth experiments was closure. To confirm that crack closure was not artificially increasing the critical and threshold stress intensities measured, closure measurements were made during a fatigue crack growth test at room temperature. An extensometer strapped to a pair of bolts set in the specimen face was used to measure displacement at crack length intervals of 0.1 mm, and the corresponding values of crack opening displacement (COD) were calculated. Fig. 10 shows the measured COD vs. load applied over an individual cycle at crack lengths of 4.64 mm, 5.15 mm, and 5.80 mm. These curves show no deviation from linearity, indicating that no measurable crack closure was observed. These results also indicate that there is little plasticity during stable crack growth. At long crack lengths just prior to failure a slight curvature of the COD vs.

load line at high loads was observed. This indicates the onset of plasticity and plane stress conditions just prior to catastrophic failure. The specimen compliance determined from the COD measurements demonstrated the expected increase as crack length increased.

Fractography of FCG Specimens

After failure, the fracture surfaces of fatigue crack growth specimens were examined in an AMR-1000 scanning electron microscope (SEM) and the fracture mode (cleavage, transgranular dimples, intergranular, striations, etc.) noted. The fracture surfaces were cut off the rest of the failed specimen on a cut-off wheel, and mounted on an aluminum SEM mount using cement. A carbon-based paint was used to paint over the CT specimen-mount junction to ensure electrical conductivity and eliminate difficulties with specimen charging. The SEM was used with a working distance of 12 mm and an accelerating voltage of 20 kV. All SEM photographs were taken with Polaroid no. 55 film.

The fracture surfaces of B2 ordered FA-129 were predominantly transgranular, with a dimpled appearance in oxygen at 25°C (Fig. 11), and in air at 150 °C (Fig.12), suggesting a microvoid coalescence mechanism. Occasional striations can be seen in Fig. 12, with the striation spacing being larger than the corresponding value of da/dN. These striations appear to have a cleavage nature. In the more aggressive environments (room temperature air and hydrogen gas) the fracture surface exhibits more pronounced cleavage facets. Fig. 13 shows the fracture surface of B2 ordered FA-129 in air at 25°C, and Fig. 14 shows the fracture surface of B2 ordered FA-129 in H_2 at 25°C.

DO_3 ordered FA-129 exhibits a shift in fracture mode at room temperature. In oxygen the surface is transgranular with a dimpled appearance, again suggesting microvoid coalescence (Fig. 15). In air (Fig. 16) and hydrogen gas (Fig. 17) the surface shows a mix of intergranular and transgranular cleavage failure. The fracture surface in air at temperatures of 150°C - 450°C become predominantly transgranular. Fig. 18 shows the fracture surface of DO_3 ordered FA-129 fatigued in air at 450°C. Widely spaced striations were observed in the DO_3 ordered material fatigued at elevated temperature. As in the B2-ordered material, these striations do not correspond to single-cycle crack increments.

The fracture surface of alloy FAP-Y shows a transgranular appearance in both air (Fig. 19) and oxygen (Fig. 20). The similarity of the fracture surfaces in air and oxygen is consistent with the similarity between the crack growth curves measured in these two environments.

Transmission Electron Microscopy of FCG Specimens

FA-129 CT specimens tested in fatigue crack growth experiments were analyzed by transmission electron microscopy to characterize the microstructure and dislocation structure of these specimens, and to compare changes when tested in fatigue in various environments. This work was done under the SHaRE program with the aid of SHaRE contact Dr. P.J. Maziasz. TEM thin foils were prepared at RPI and examined at ORNL on a 300 kV Phillips TEM. The foils were cut from the fatigued regions of specimens of both B2 and DO_3 ordered conditions tested in a variety of environments. Foils far from the fatigue zone and from untested material also were prepared as control specimens.

The foils were prepared by slicing off a thin section of the fracture surface on a diamond-blade cutoff wheel or wire-slurry saw. The fracture surface was carefully ground on a slowly revolving polishing wheel with 240 grit paper as far as required to create a smooth surface, typically 0.2 - 0.4 mm. The opposite face was then ground in a similar manner until the total thickness was approximately 0.3 mm. The circular foils were then removed by cutting out 3.0 mm diameter disks with a slurry disk drill. These disks were mechanically ground on both sides with 400 and 600 grit paper, until a thickness of 150 μm was reached. The disks were then electropolished to perforate them using a Ficshione jet-polisher. The electrolytic solution consisted of 6% perchloric acid in methanol. The jet-polisher parameters were as follows: 100 mA current, -20°C temperature, and 30-60 seconds of polishing time. All TEM photographs were taken using Kodak Ectar high density electron microscope film.

The B2 ordered specimens showed a duplex microstructure: predominantly unrecrystallized with a cellular subgrain structure (see Fig. 21). However, some recrystallized regions were observed with a lower dislocation density, more paired dislocation, and APB's.

The DO_3 specimens exhibited few or no subgrains, a much lower dislocation density than the B2 material, and a uniform network of APB's, as seen in Fig. 22. The dislocations which were observed were also more likely to be paired than in the B2 material. The DO_3 grain boundaries tended to be free of dislocations while the B2 material often had dense dislocation networks emanating from the grain boundaries.

Heterogeneously distributed coarse precipitates (up to 5 μm diameter), which were believed to be niobium carbides, were observed. The precipitates often acted as dislocation sources, possibly as a result of mismatched thermal contraction during quenching. These precipitates are seen in the optical micrograph in Fig. 1(d).

Diffraction patterns were obtained from all samples, and from these it was determined that the proper ordered state (B2 or DO_3) was achieved in each case.

Environment and test temperature both affected the dislocation density observed in FA-129. Increased numbers of dislocations in both ordered states were observed as the environment changed through hydrogen, air, and oxygen. In both ordered states, much higher dislocation densities were observed at elevated temperatures than at room temperature, and large arrays of dislocations were also observed (Fig. 23), sometimes forming subgrains or cells. Microscopy on foils taken away from the fracture surface, and from untested material, showed extremely few dislocations. This confirms that there was no significant damage induced in the foils during the preparation process.

TEM analysis of fatigued FAP-Y indicates a much lower dislocation density than in FA-129, which is consistent with the lower fatigue crack growth resistance measured in FAP-Y. Figs. 24 and 25 show the dislocation structures of FAP-Y fatigued in air and oxygen, respectively. Note the small round structures in Fig. 25 which may be dislocation loops. As with the FA-129, foils of unfatigued FAP-Y also were studied to determine the initial fatigue structure. Fig. 26 shows an unfatigued FAP-Y microstructure with nearly no dislocations and a precipitate situated at a grain boundary. Note also the absence of the dislocation loops which were seen in the fatigued FAP-Y (Fig. 25)

FAP-Y shows a precipitate distribution similar to that seen in alloy FA-129. However, the precipitates are of various types, as EDAX chemical analysis shows. The predominant precipitates are zirconium carbides (shown in Fig. 27 with the corresponding EDAX analysis) and Laves phases (shown in Fig. 28 with the corresponding EDAX analysis).

Tensile Tests

A series of tensile tests were conducted on alloys FA-129 and FAP-Y. Alloy FA-129 was tested in air, vacuum, and oxygen at temperatures of 25°C, 150°C, and 600°C for the B2 state, and at 25°C, 150°C, 300°C, and 450°C in the DO_3 state. The FA-129 specimens were punched from 0.76 mm thick plate at ORNL and sent to RPI for testing. The gauge sections were 12.7 mm x 3.2 mm x 0.76 mm thick. The specimens were pin loaded and tested in a servo-hydraulic MTS machine. The tensile tests were run in stroke control with the stroke feedback signal used as a measure of displacement. All tensile specimens were polished to a 0.3 μm finish and ultra-sonically cleansed in acetone prior to testing. The strain rate used in all tests was 3.3×10^{-4} /sec. Results at 25°C represent the average of two tests, and all others represent single tests. The procedures for testing in gaseous environments which were previously described for FCG tests also were used in the tensile tests. A summary of the results is shown in Table III.

Table III - Tensile Data for FA-129

		Air			Vac			O_2		
Order	Temp	Duct.	YS	UTS	Duct.	YS	UTS	Duct.	YS	UTS
B2	25 °C	8.8	409	677	13.7	412	859	16.2	440	858
	150 °C	16.7	369	865	16.5	409	885	23.4	417	936
	600 °C	30.7	303	351	38.5	293	392	41.8	306	416
DO_3	25 °C	3.4	495	645	4.8	547	897	5.8	580	904
	150 °C	15.2	415	846	16.9	414	938	23.1	436	958
	300 °C	29.3	367	934	27.0	420	977	29.5	423	987
	450 °C	24.2	369	683	25.5	412	679	26.2	420	717

ductility = plastic strain at failure in %, YS and UTS in MPa

As expected, ductility and UTS are greatly increased at room temperature by testing in vacuum and oxygen. In addition, a large increase in ductility and UTS is found when increasing the temperature of the tests from 25°C to 150°C. At all temperatures ductility is considerably higher in the B2 than in the DO_3 condition

Tensile tests were performed on FAP-Y in hydrogen gas, air, and oxygen at 25°C. The FAP-Y tensile bars were machined from 5.08 mm thick plate. The gauge section dimensions of these specimens were as follows: 12.7 mm x 3.17 mm x 1.90 mm. The testing procedure was otherwise identical to that of the FA-129 tensile tests. The results of the FAP-Y tensile tests are tabulated in Table IV.

Table IV - Tensile Properties of Alloy FAP-Y at 25°C

Environment	Ductility (%)	YS (MPa)	UTS (MPa)
Hydrogen	6.3	484	614
Air	25.5	487	665
Oxygen	24.0	498	653

ductility = plastic strain at failure in %, YS and UTS in MPa

FA-129 clearly shows the effect of moisture in air and gaseous hydrogen on ductility and UTS. FAP-Y also shows embrittlement in gaseous hydrogen, but there appears to be little effect on ductility and fracture toughness in air. Alloy FA-129 exhibits a great deal of strain hardening, and therefore the UTS is reduced as ductility is reduced when tested in air, because less strain hardening occurs. This effect is not seen in alloy FAP-Y, which exhibits very little strain hardening. Fig. 29 shows a comparison of the ductility measured in the alloys FA-129 and FAP-Y. FAP-Y exhibits similar ductility in both air and oxygen

(25.5% and 24.0% respectively), but exhibits a dramatic decrease in ductility in hydrogen (down to 6.3%).

Figs. 30-32 show the fracture surfaces of alloy FAP-Y tensile tested in gaseous hydrogen, air, and oxygen respectively. The change from transgranular cleavage in hydrogen gas (Fig. 30) to mixed transgranular cleavage and dimples in air and oxygen (Figs. 31 and 32) is clear. In alloy FA-129, there is a change in fracture surface when the environment is changed from air to oxygen. Fig. 33 shows a mixed transgranular-intergranular surface in B2 ordered FA-129 tested in air, while Fig. 34 shows the predominantly transgranular surface for B2 ordered FA-129 tested in oxygen.

Summary

Alloy FA-129 undergoes an increase in crack propagation rate and a loss of fracture toughness in moisture-bearing and hydrogen gas environments. A similar effect is seen on ductility of FA-129 in tensile tests. The embrittling effect in air is attributed to oxidation of aluminum in the alloy by water vapor to produce Al_2O_3 and hydrogen gas. Alloy FAP-Y, which is disordered and contains only 16 a%Al is embrittled by hydrogen gas in a manner similar to that of FA-129. However, laboratory air had little effect on the crack growth rates, fracture toughness, or tensile ductility. The lower aluminum content apparently is insufficient to induce the Al-H_2O reaction. TEM and SEM analyses of microstructure and fracture surfaces were consistent with the change in fracture toughness with order and environment. Testing at elevated temperatures reduces crack growth rates in FA-129, and increases fracture toughness and ductility. This is consistent with the well documented peak in hydrogen embrittlement in structural alloys at or near room temperature. Elevated temperature affects the degree of embrittlement in a complex manner, possibly changing the rates of several of the processes involved.

Acknowledgments

The authors are grateful to the Department of Energy, Fossil Energy Program for providing financial support under Martin Marietta Energy Subsystems. Subcontract No. 19X-SF521C. Assistance also was provided by the Oak Ridge National Laboratory SHaRE program and Dr. P.J. Maziasz. The authors also are grateful for helpful discussion with Drs. C.T. Liu and V.K. Sikka of ORNL and to Dr. Sikka for provision of test alloys.

References

1) C.G. McKamey, J.H. DeVan, P.E. Tortorelli, and V.K. Sikka; *J. Material Research* 6, p. 1779 (1991)

2) M. Shea, A. Castagna, and N.S. Stoloff in High Temperature Ordered Intermetallics IV, MRS Symp. Proc., vol. 213, p. 609 (1991)

3) C.T. Liu, H.E. Lee, and C.G. McKamey; *Scripta Met.* 23, p.875 (1989)

4) C.G. McKamey, J.A. Horton, and C.T. Liu; *J. Material Research* 4, p. 1156 (1989)

5) D.B. Kasul and L.A. Heldt; in Environmental Effects on Advanced Materials, TMS, Warrendale PA, p. 67 (1991)

6) R.J. Lynch, L.A. Heldt, and W.W. Milligan, *Scripta Met.* 25, p. 2147 (1991)

7) C.G. McKamey and C.T. Liu; *Scripta Met.* 24, p.2119 (1990)

Figures

(a)

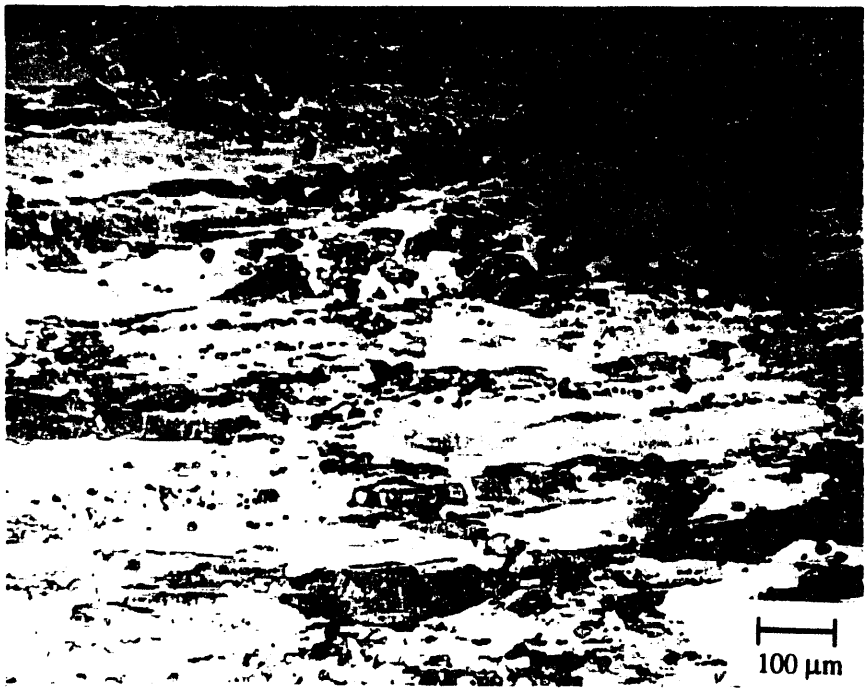

(b)

Fig. 1) Grain structure in the longitudinal direction of as received FA-129 (a) and B2 ordered FA-129 (b).

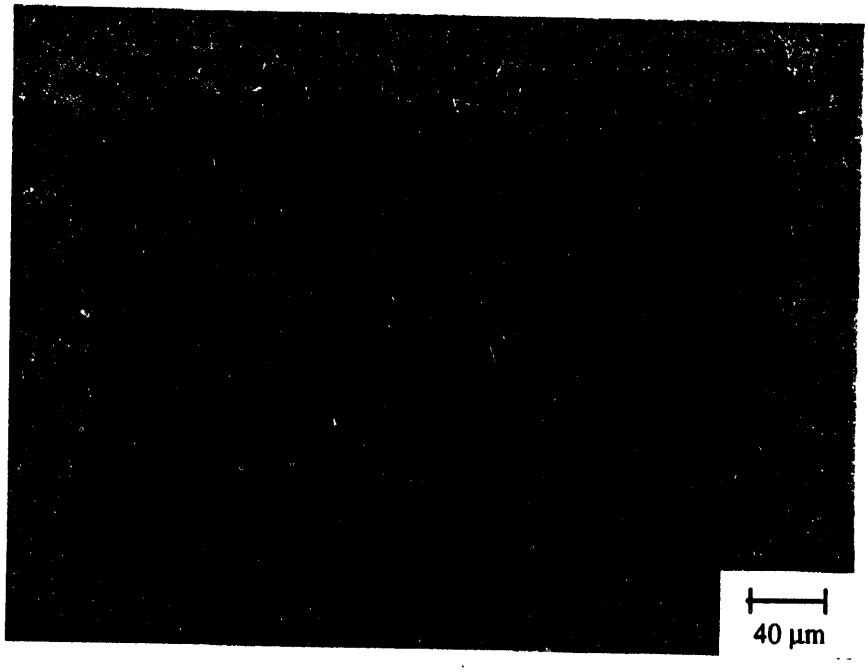

(c)

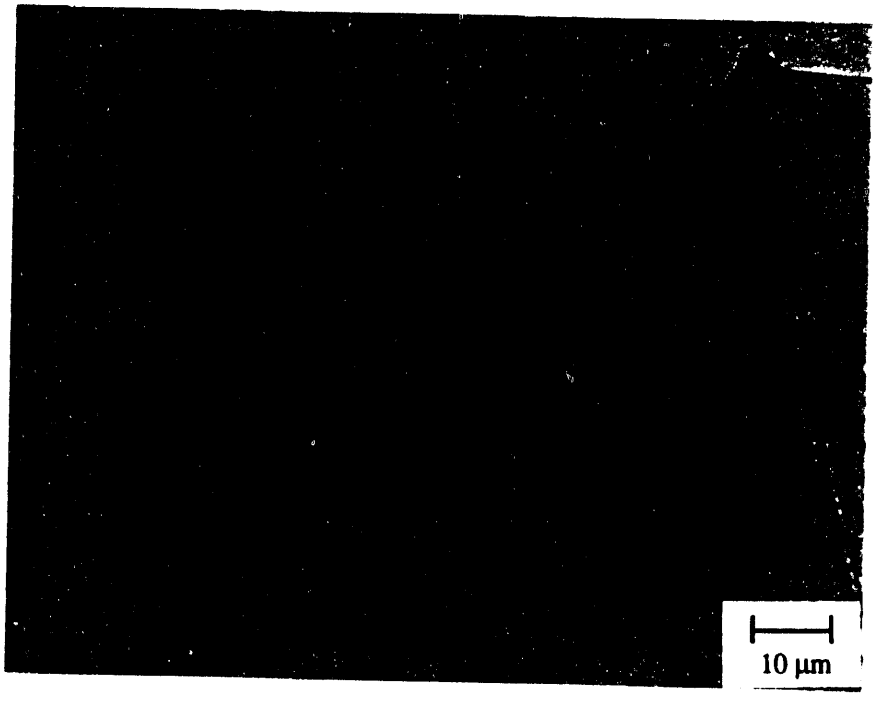

(d)

Fig. 1, continued) Grain structure in the longitudinal direction of DO_3 ordered FA-129 (c), and B2 ordered FA-129 showing precipitates (d).

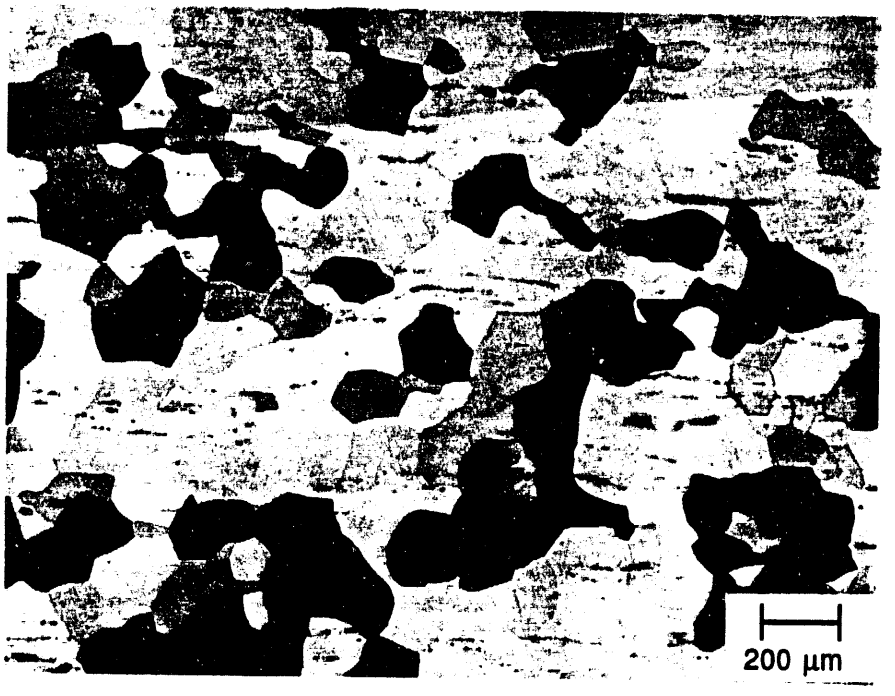

Fig. 2) Grain structure of B2 ordered FA-129 utilizing a 900°C + 700°C anneal.

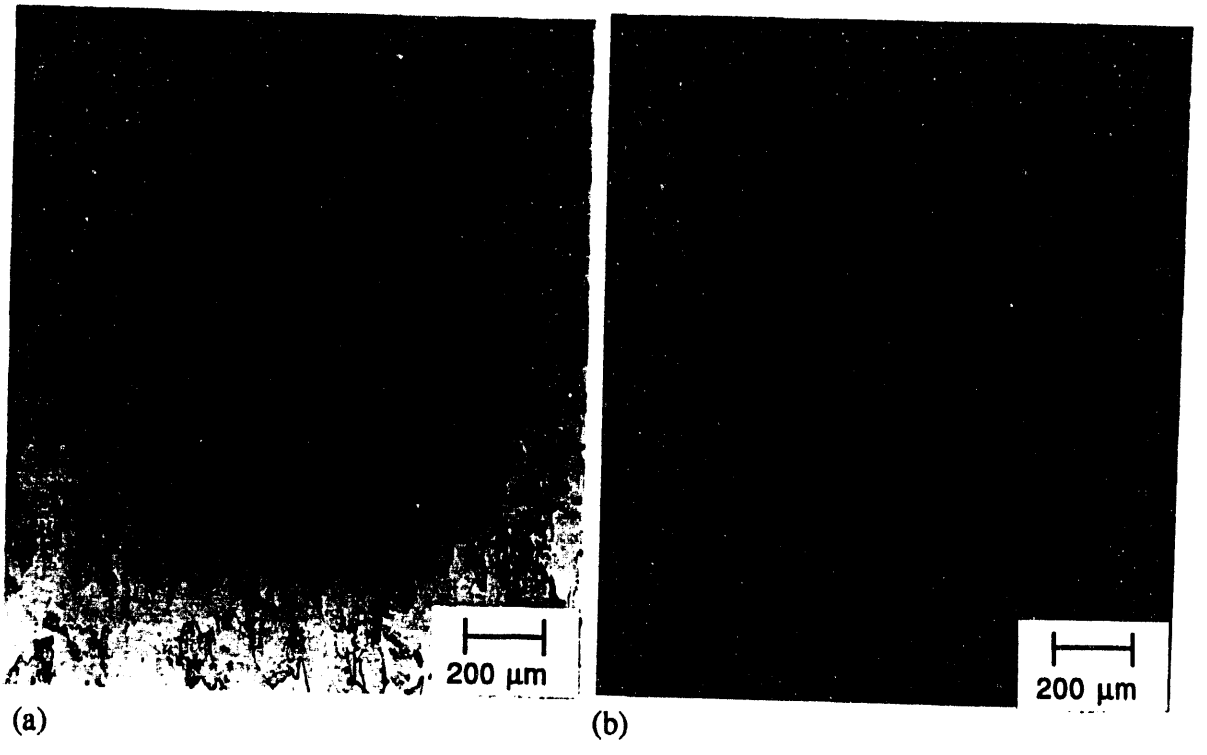

Fig. 3) Grain structure in as received FAP-Y (a) and annealed FAP-Y (b).

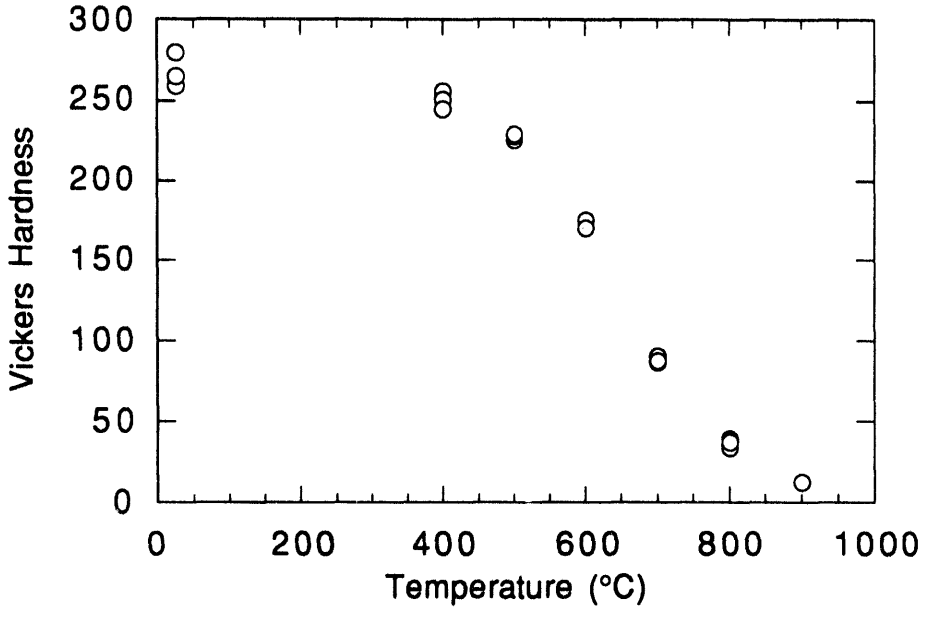

Fig. 4) Vickers hot hardness measurements of alloy FA-129.

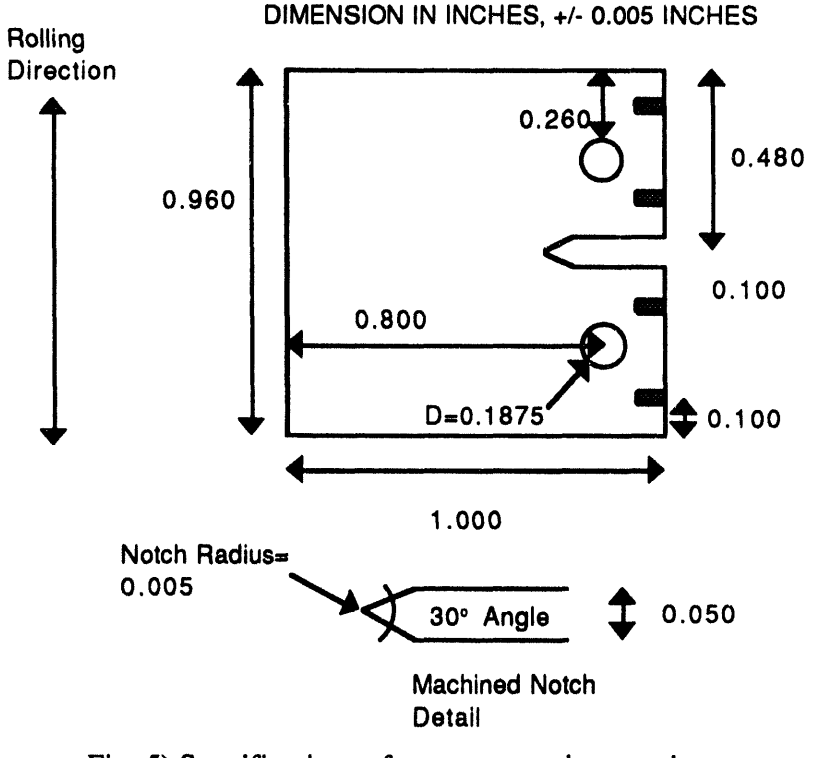

Fig. 5) Specifications of compact tension specimen.

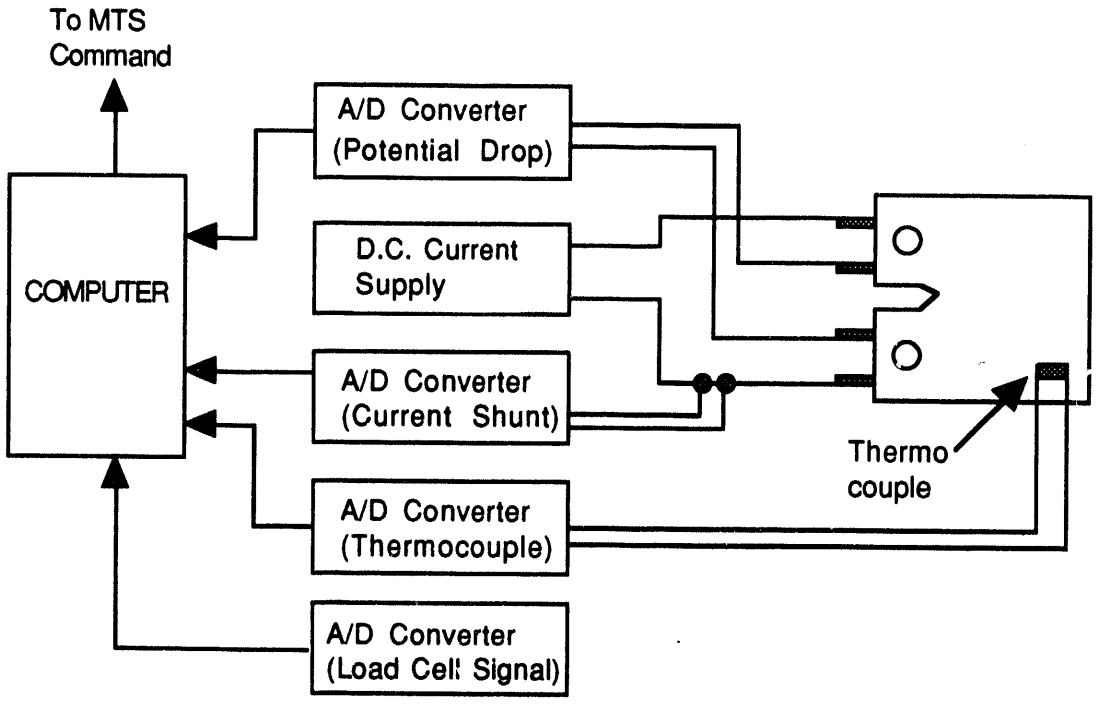

6) Instrumentation set-up for d.c. potential drop system.

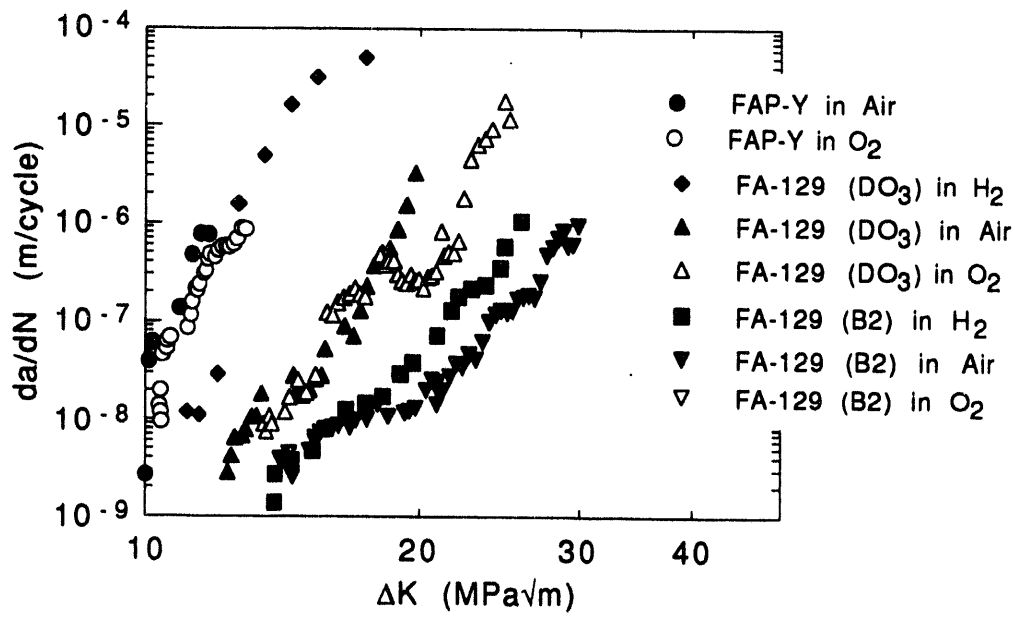

Fig. 7) Fatigue crack growth curves for FA-129 and FAP-Y at 25°C.

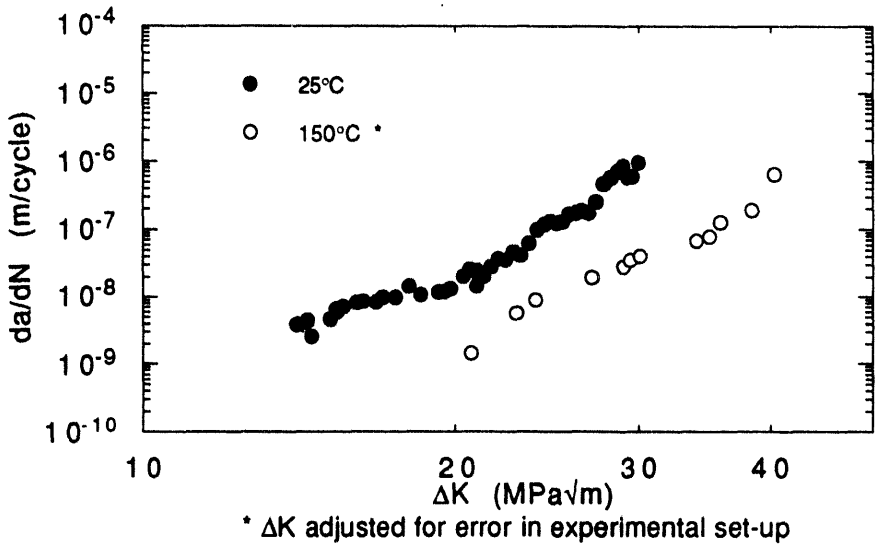

Fig. 8) Fatigue crack growth curves in B2 ordered FA-129 in air at various temperatures.

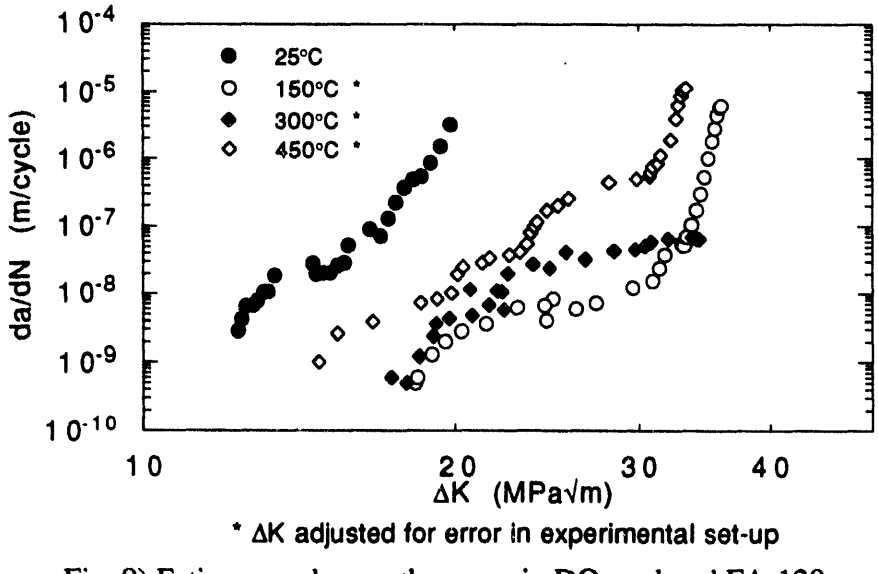

Fig. 9) Fatigue crack growth curves in DO_3 ordered FA-129 in air at various temperatures.

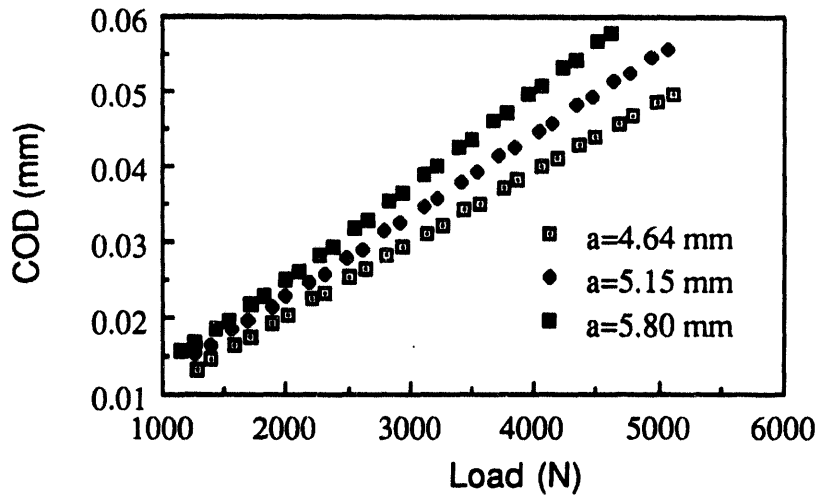

Fig. 10) Crack opening displacement vs. load at crack lengths of 4.64mm 5.15mm, and 5.80 mm. Material is B2 ordered FA-129 in air at 25°C.

Fig. 11) Fracture surface of B2 ordered FA-129 fatigued in oxygen at 25°C.

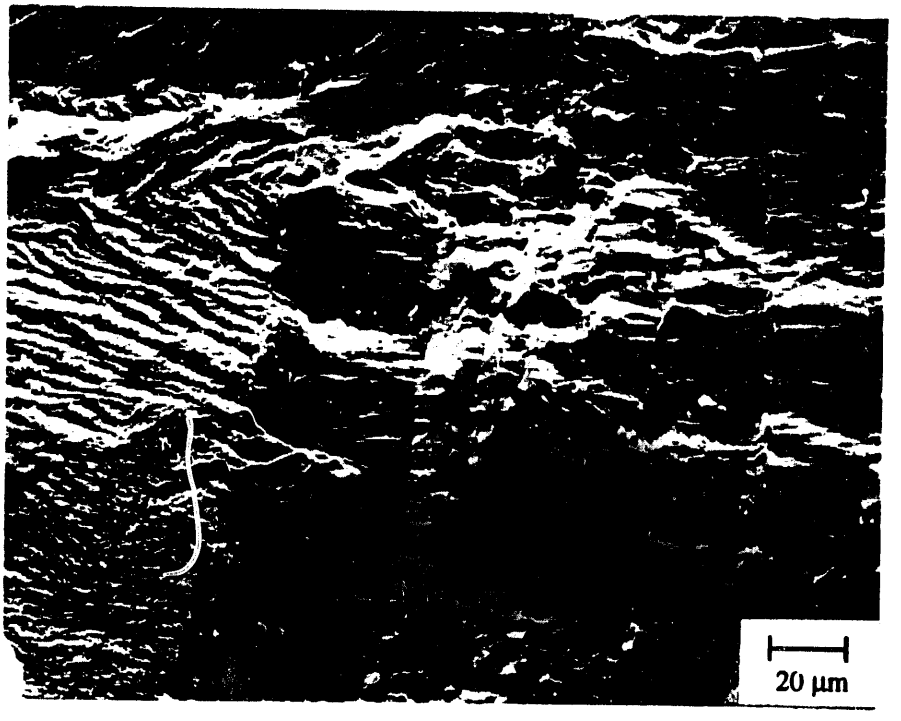

Fig. 12) Fracture surface of B2 ordered FA-129 fatigued in air at 150°C.

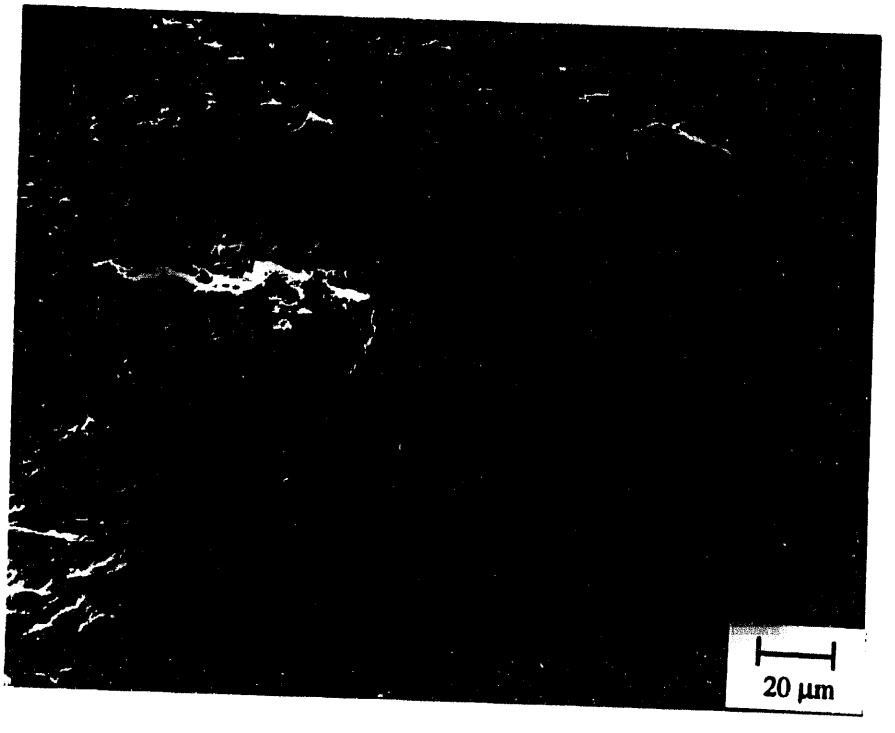

Fig. 13) Fracture surface of B2 ordered FA-129 fatigued in air at 25°C.

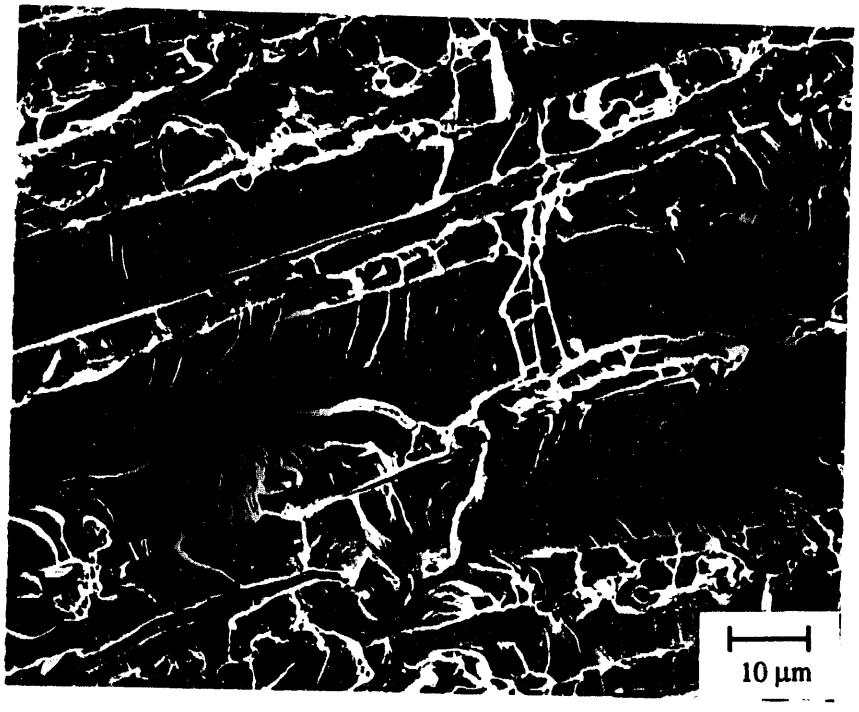

Fig. 14) Fracture surface of B2 ordered FA-129 fatigued in hydrogen at 25°C.

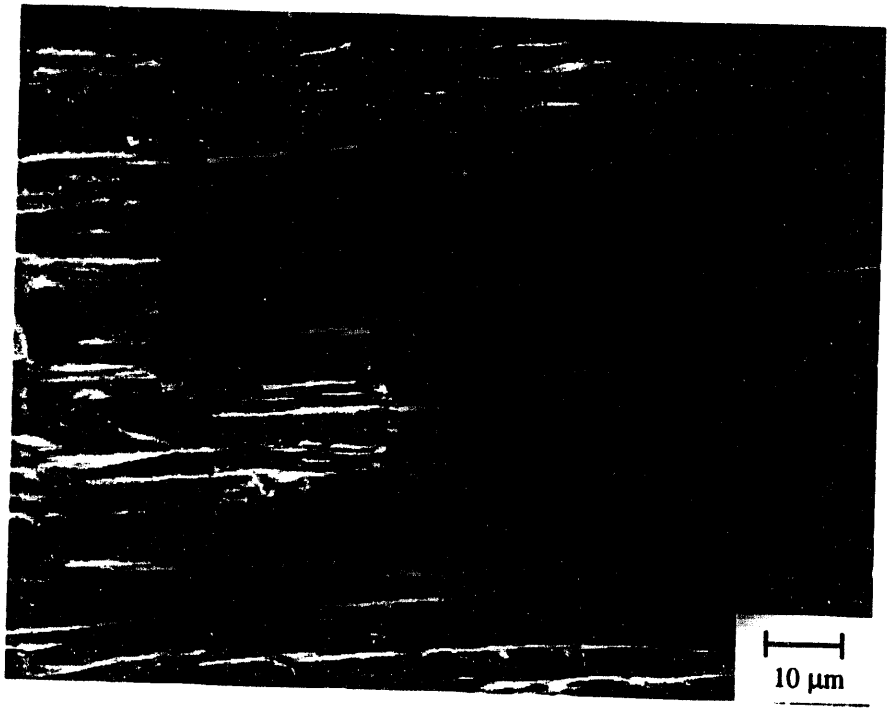

Fig. 15) Fracture surface of DO_3 ordered FA-129 fatigued in oxygen at 25°C.

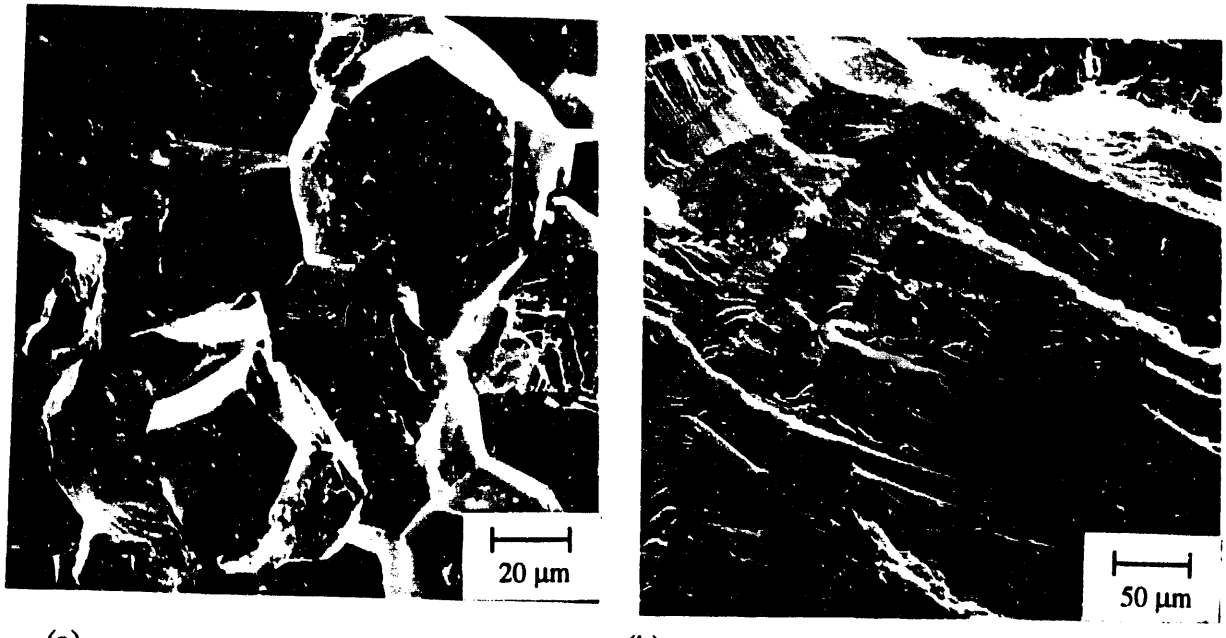

(a) (b)

Fig. 16) Fracture surface of DO_3 ordered FA-129 fatigued in air at 25°C showing IG fracture (a) and TG fracture (b).

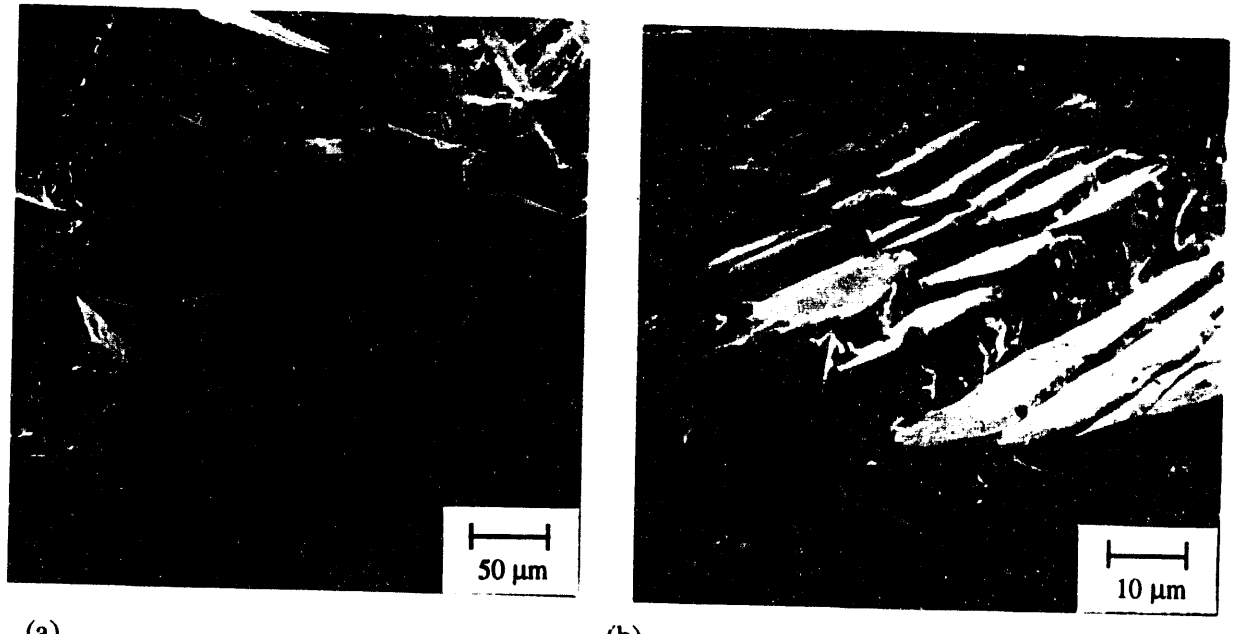

(a) (b)

Fig. 17) Fracture surface of DO_3 ordered FA-129 fatigued in hydrogen at 25°C showing IG fracture (a), and TG fracture (b).

Fig. 18) Fracture surface of DO_3 ordered FA-129 fatigued in air at 150°C.

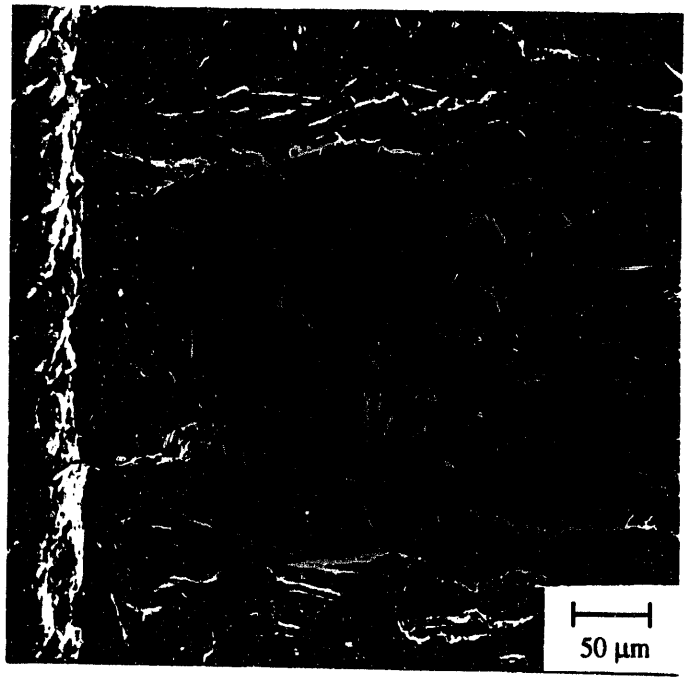

Fig. 19) Fracture surface of FAP-Y fatigued in oxygen at 25°C.

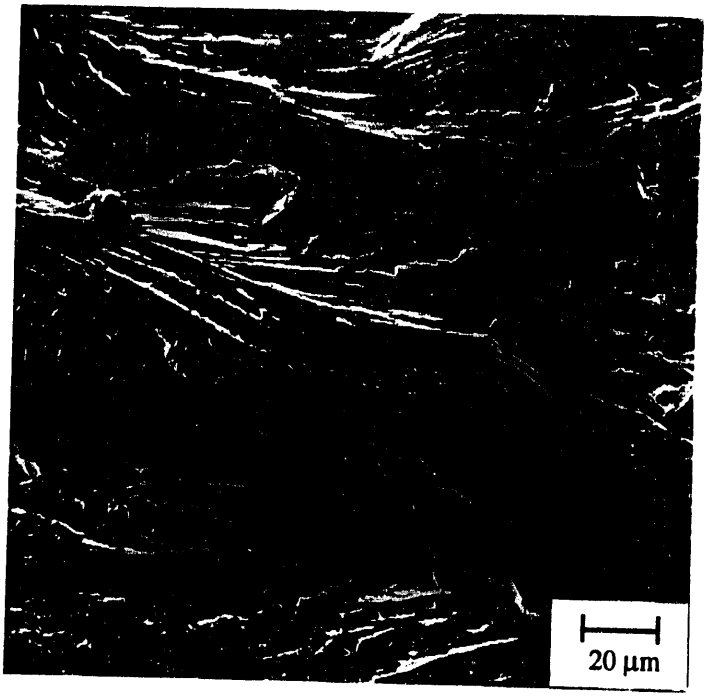

Fig. 20) Fracture surface of FAP-Y fatigued in air at 25C.

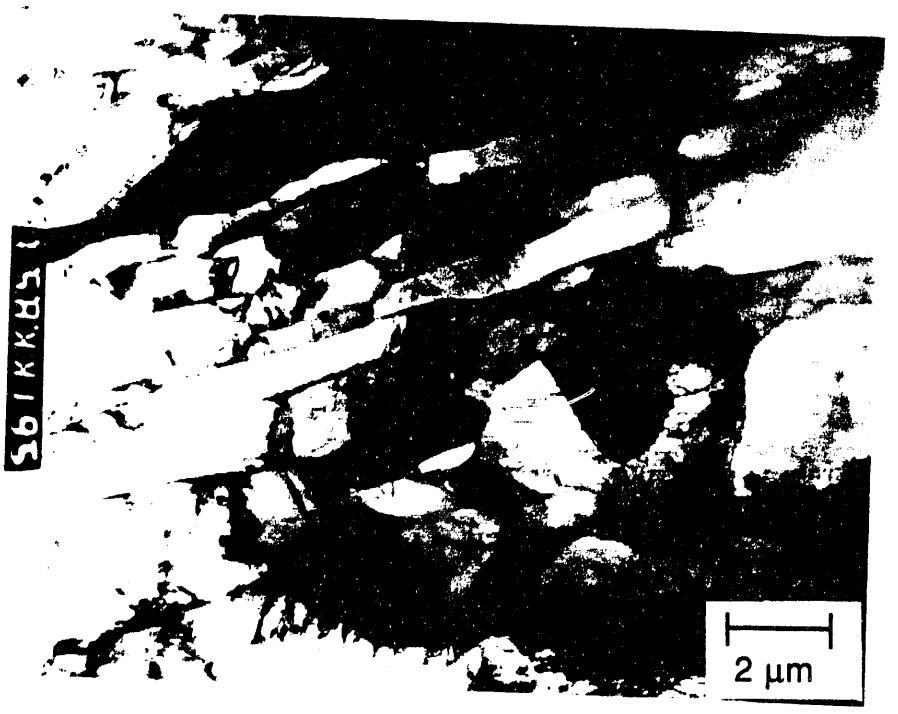

Fig. 21) Subgrains in B2 ordered FA-129 fatigued in air at 25°C.

Fig. 22) APB's in DO_3 Ordered FA129 fatigued in hydrogen at 25°C.

Fig. 23) Dislocation array in DO_3 ordered FA129 fatigued in air at 450°C.

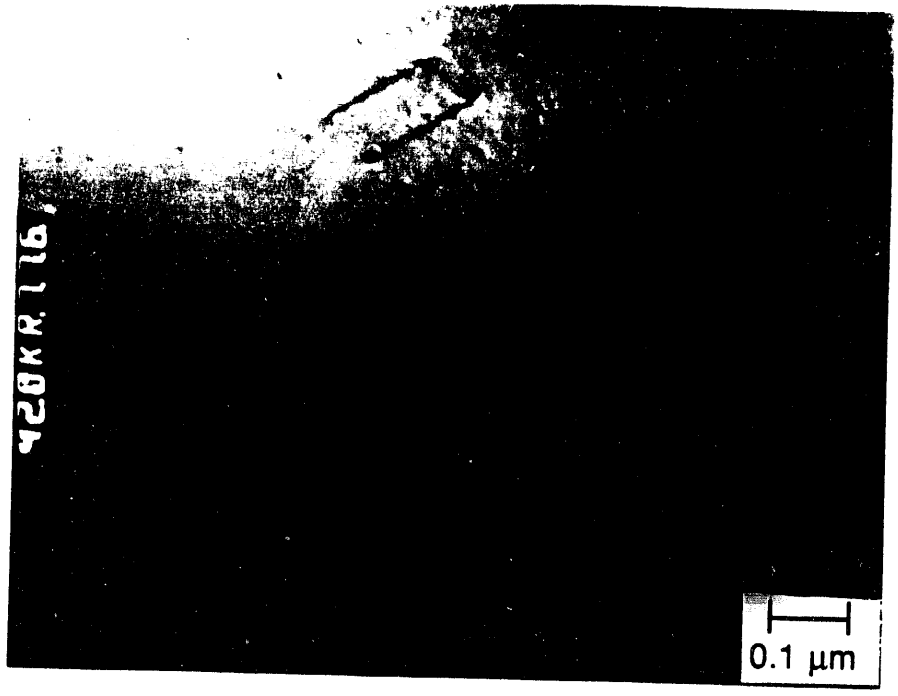

Fig. 24) Dislocation structure of FAP-Y fatigued in air at 25°C.

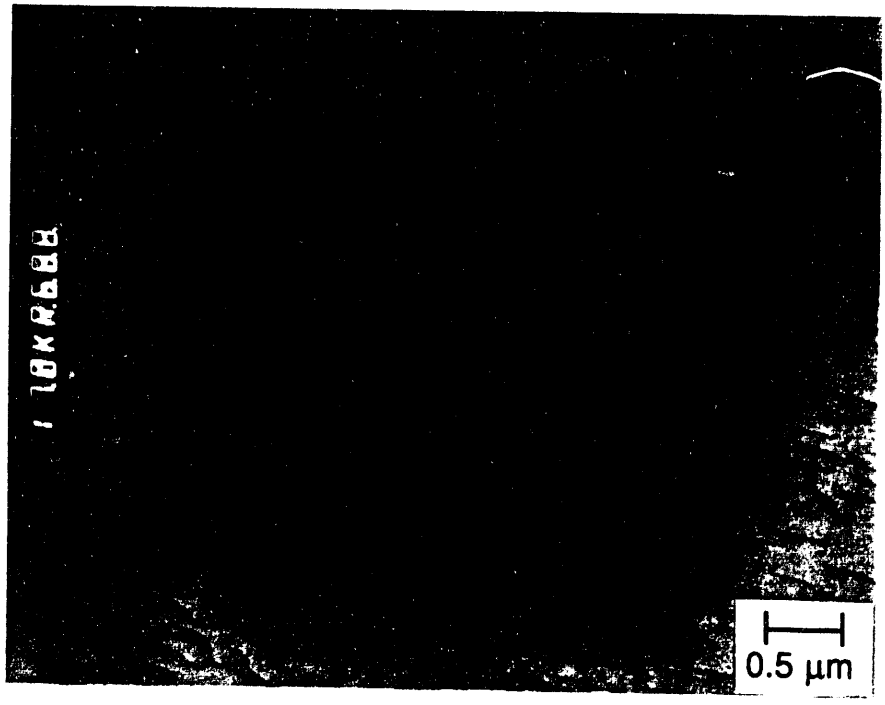

Fig. 25) Dislocation structure of FAP-Y fatigued in oxygen at 25°C.

Fig. 26) Undeformed structure of FAP-Y, showing precipitate at grain boundary.

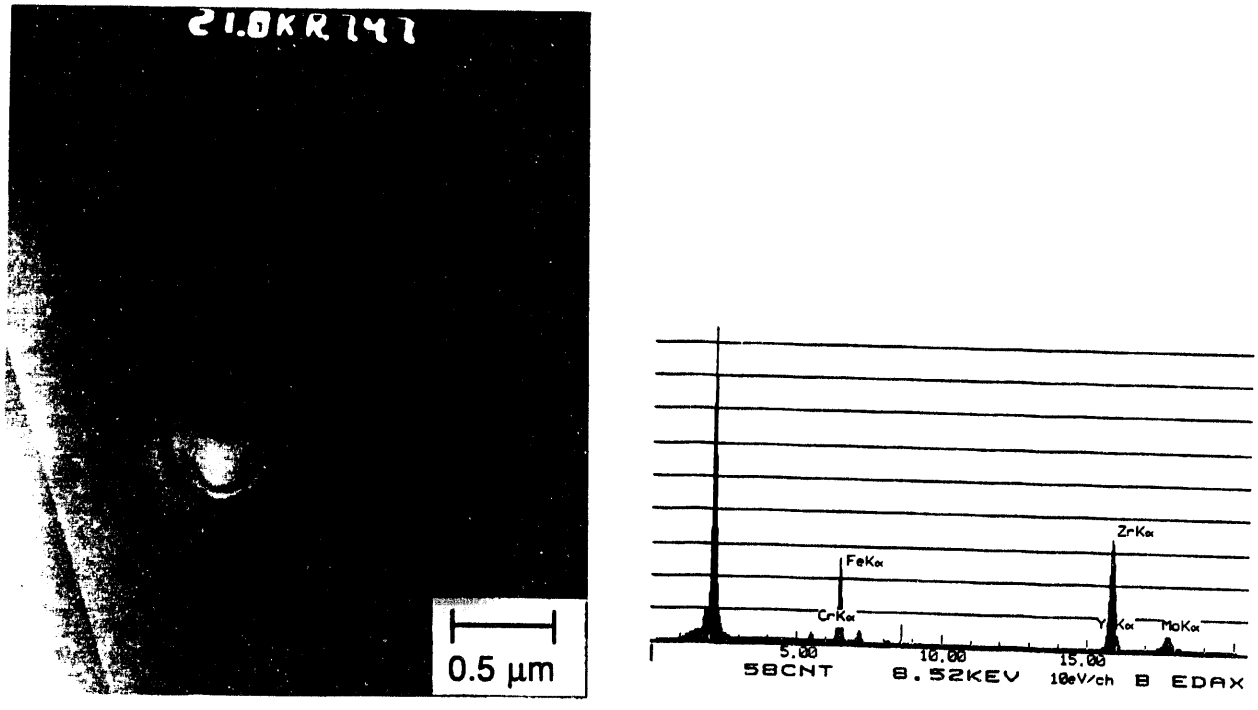

Fig. 27) ZrC precipitates in FAP-Y fatigued in air at 25°C, with correspond EDAX pattern.

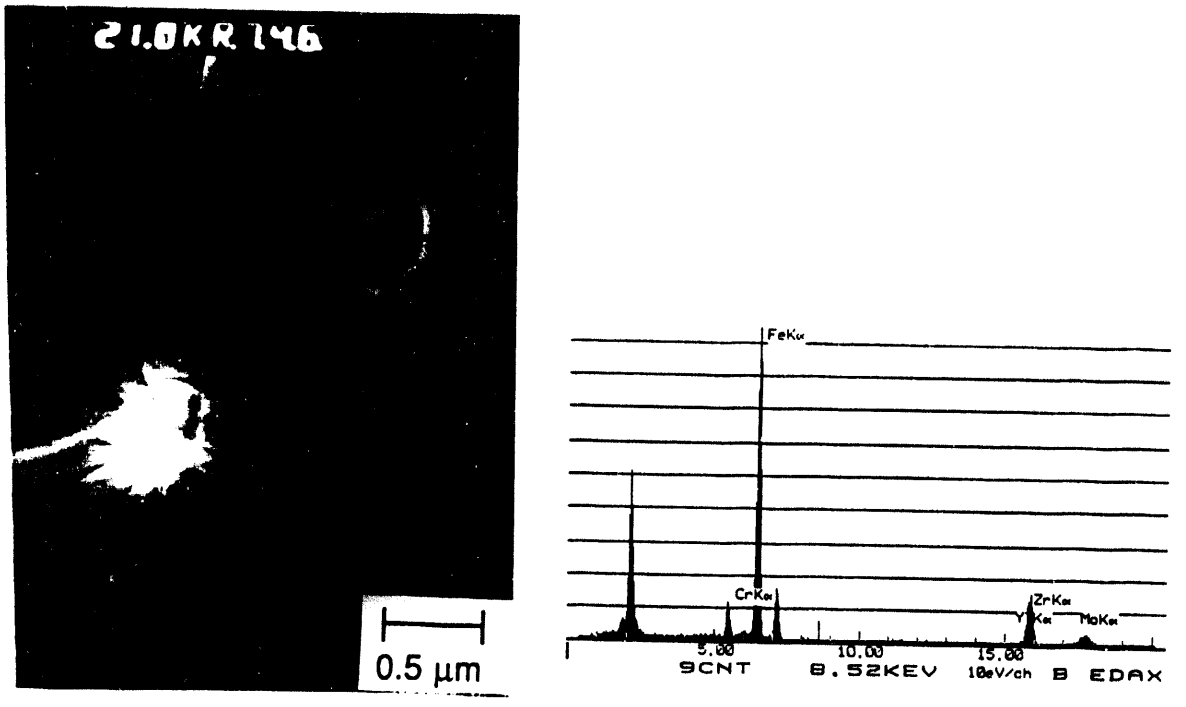

Fig. 28) Laves phase precipitates in FAP-Y fatigued in air at 25°C, with correspond EDAX pattern.

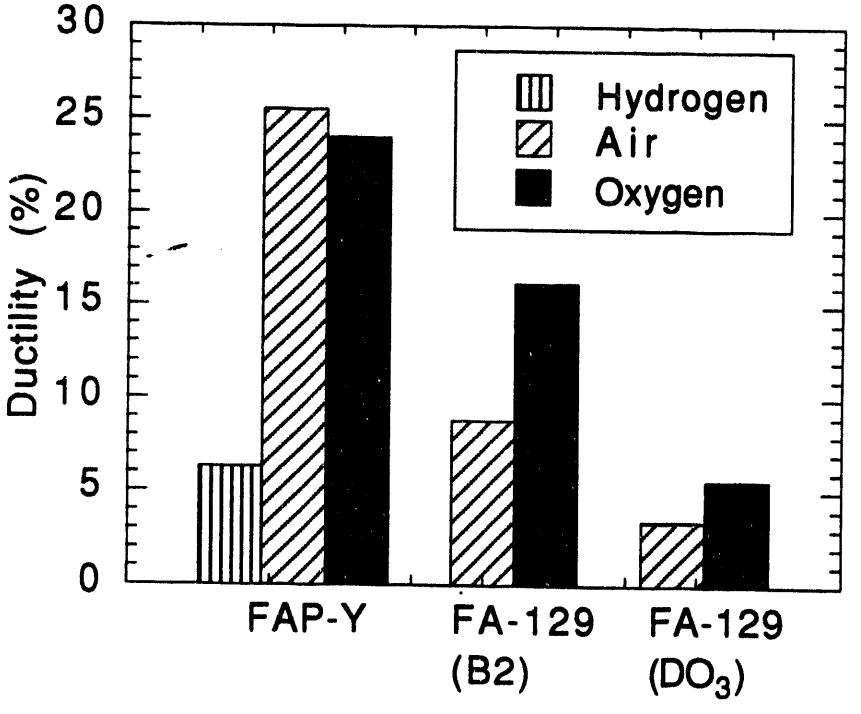

Fig. 29) Comparison of tensile ductility in FAP-Y and FA-129 at 25°C.

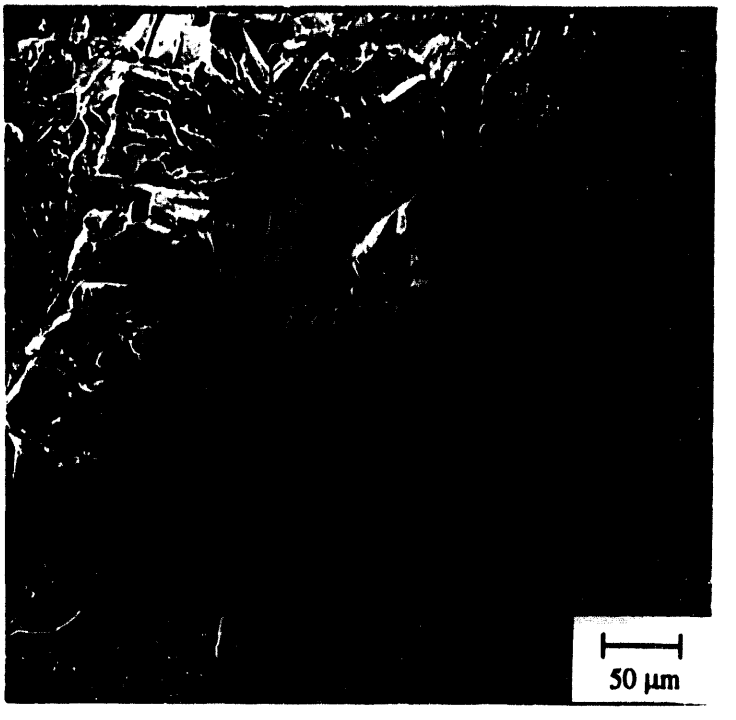

Fig. 30) Fracture surface of FAP-Y tested in tension in hydrogen at 25°C.

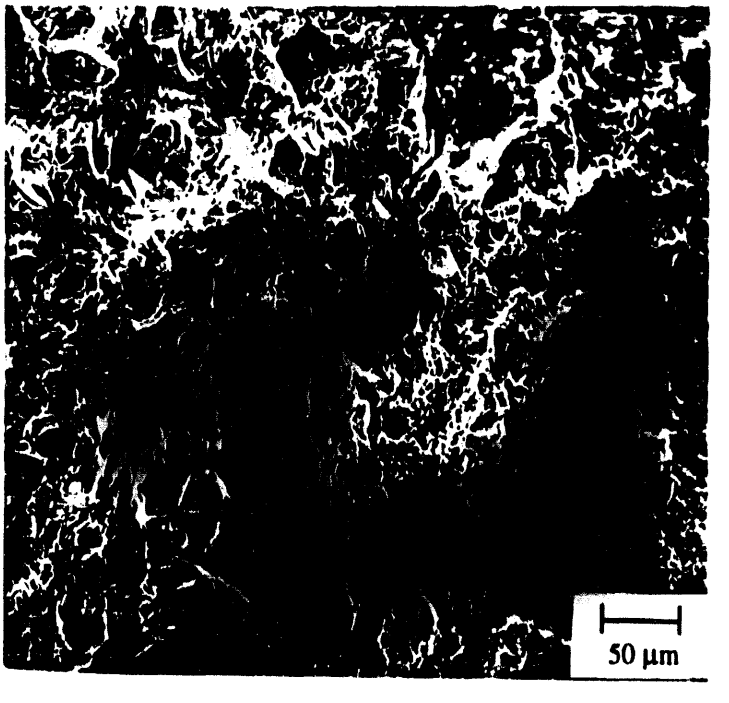

Fig. 31) Fracture surface of FAP-Y tested in tension in air at 25°C.

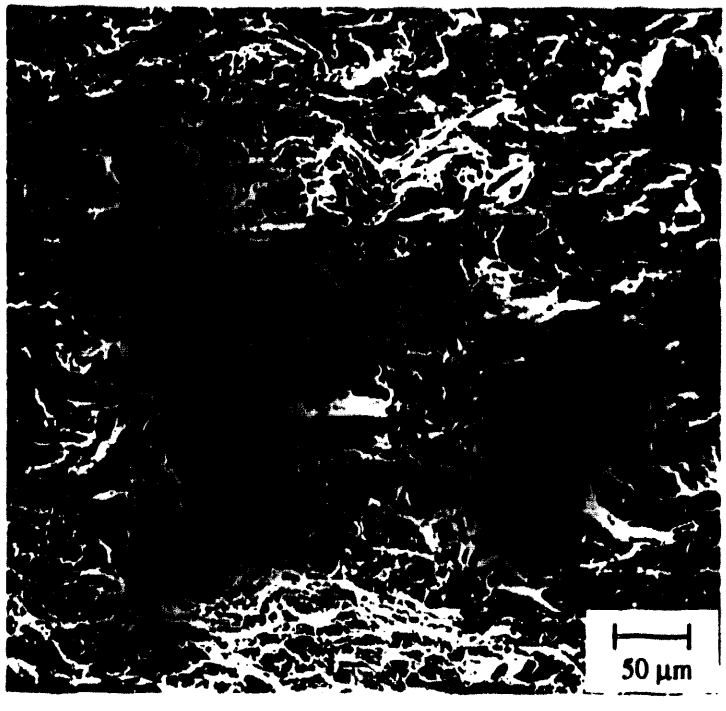

Fig. 32) Fracture surface of FAP-Y tested in tension in oxygen at 25°C.

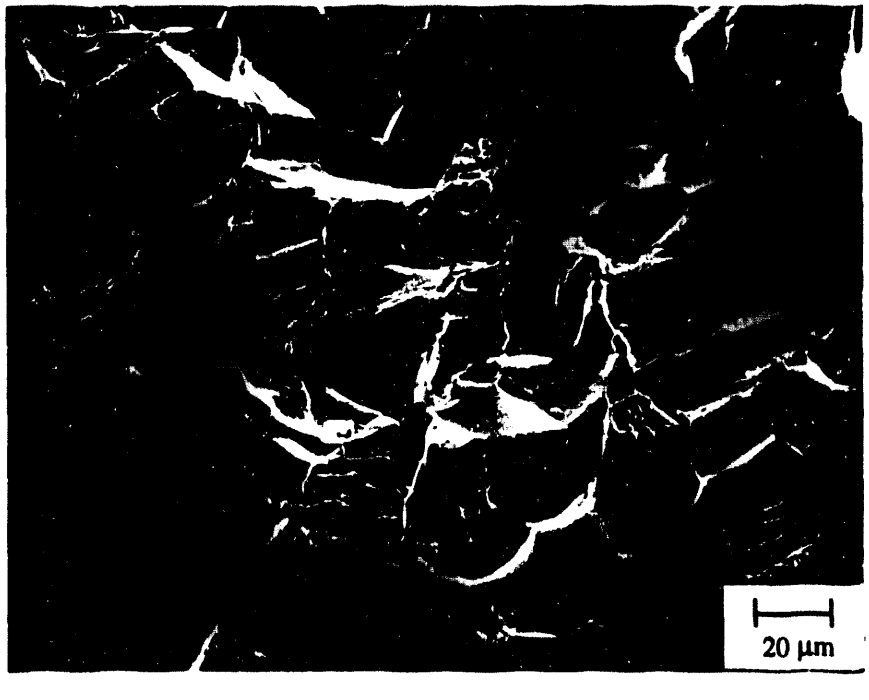

Fig. 33) Fracture surface B2 ordered FA-129 tested in tension in air at 25°C.

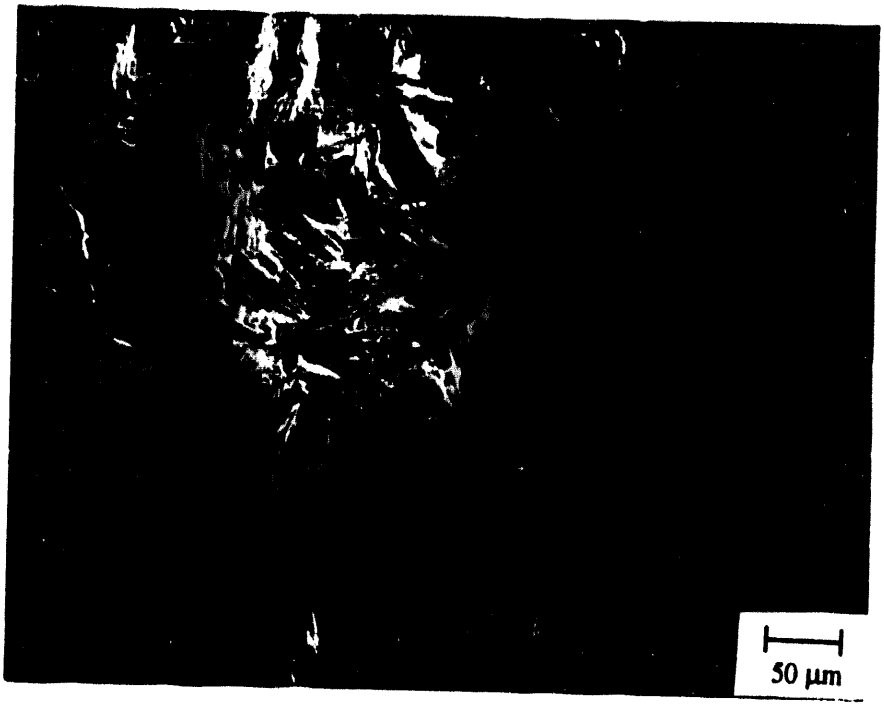

Fig. 34) Fracture surface of B2 ordered FA-129 tested in tension in oxygen at 25°C.

DISTRIBUTION

AIR PRODUCTS AND CHEMICALS
P.O. Box 538
Allentown, PA 18105
S. W. Dean
S. C. Weiner

ALBERTA RESEARCH COUNCIL
Oil Sands Research Department
P.O. Box 8330
Postal Station F
Edmonton, Alberta
Canada T6H5X2
L. G. S. Gray

ALLISON GAS TURBINE DIVISION
P.O. Box 420
Indianapolis, IN 46206-0420
P. Khandelwal (Speed Code W-5)
R. A. Wenglarz (Speed Code W-16)

ARGONNE NATIONAL LABORATORY
9700 S. Cass Avenue
Argonne, IL 60439
K. Natesan

ARGONNE NATIONAL LABORATORY-WEST
P.O. Box 2528
Idaho Falls, ID 83403-2528
S. P. Henslee

AVCO RESEARCH LABORATORY
2385 Revere Beach Parkway
Everett, MA 02149
R. J. Pollina

BABCOCK & WILCOX
1562 Beeson St.
Alliance, OH 44601
T. I. Johnson
T. Modrak

BABCOCK & WILCOX
Domestic Fossil Operations
20 South Van Buren Avenue
Barberton, OH 44023
M. Gold

BATTELLE-COLUMBUS LABORATORIES
505 King Avenue
Columbus, OH 43201
I. G. Wright

BRITISH COAL CORPORATION
Coal Research Establishment
Stoke Orchard, Cheltenham
Glocestershire, England GL52 4RZ
J. Oakey

CANADA CENTER FOR MINERAL & ENERGY TECHNOLOGY
568 Booth Street
Ottawa, Ontario
Canada K1A OG1
R. Winston Revie
Mahi Sahoo

CONSOLIDATION COAL COMPANY
4000 Brownsville Road
Library, PA 15129
S. Harding

ELECTRIC POWER RESEARCH INSTITUTE
P.O. Box 10412
3412 Hillview Avenue
Palo Alto, CA 94303
W. T. Bakker
J. Stringer
R. H. Wolk

EUROPEAN COMMUNITIES JOINT RESEARCH CENTRE
Petten Establishment
P.O. Box 2
1755 ZG Petten
The Netherlands
M. Van de Voorde

FLUIDIZED BED TECHNOLOGIES
P. O. Box 4469
Chattanooga, TN 37405
R. Q. Vincent

FOSTER WHEELER DEVELOPMENT CORPORATION
Materials Technology Department
John Blizard Research Center
12 Peach Tree Hill Road
Livingston, NJ 07039
J. L. Blough

GAS RESEARCH INSTITUTE
8600 West Bryn Mawr Avenue
Chicago, IL 60631
H. S. Meyer

IDAHO NATIONAL ENGINEERING LABORATORY
P. O. Box 1625
Idaho Falls, ID 83415
A. B. Denison

LAWRENCE LIVERMORE LABORATORY
P.O. Box 808, L-325
Livermore, CA 94550
W. A. Steele

MOBIL RESEARCH & DEVELOPMENT CORPORATION
P. O. Box 1026
Princeton, NJ 08540
R. C. Searles

NATIONAL MATERIALS ADVISORY BOARD
National Research Council
2101 Constitution Avenue
Washington, DC 20418
K. M. Zwilsky

NEW ENERGY AND INDUSTRIAL TECHNOLOGY DEVELOPMENT ORGANIZATION
Sunshine 60 Bldg.
P.O. Box 1151
1-1, Higashi-Ikebukuro 3-chrome
Toshima-Ku, Tokyo, 170
Japan
H. Narita
S. Ueda

OAK RIDGE NATIONAL LABORATORY
P.O. Box 2008
Oak Ridge, TN
D. J. Alexander
P. T. Carlson
N. C. Cole
J. H. DeVan
R. R. Judkins
R. A. Lawson **(8 copies)**
P. T. Thornton
P. F. Tortorelli

RISOE NATIONAL LABORATORY
P.O. Box 49
DK-4000
Roskilde, Denmark
Aksel Olsen

SHELL DEVELOPMENT COMPANY
P. O. Box 1380
Houston, TX 77251-1380
L. W. R. Dicks

SOUTHWEST RESEARCH INSTITUTE
6620 Culebra Road
P.O. Drawer 28510
San Antonio, TX 78284
F. F. Lyle, Jr.

TENNESSEE VALLEY AUTHORITY
Energy Demonstration & Technology
MR 2N58A
Chattanooga, TN 37402-2801
C. M. Huang

TENNESSEE VALLEY AUTHORITY
1101 Market Street
3A Missionary Ridge
Chattanooga, TN 37402-2801
A. M. Manaker

TEXAS EASTERN TRANSMISSION CORPORATION
P.O. Box 2521
Houston, TX 77252
D. H. France

THE MATERIALS PROPERTIES COUNCIL, INC.
United Engineering Center
345 E. Forty-Seventh Street
New York, NY 10017
M. Prager

THE TORRINGTON COMPANY
Advanced Technology Center
59 Field Street
Torrington, CT 06790
W. J. Chmura

UNIVERSITY OF TENNESSEE AT KNOXVILLE
Materials Science and Engineering Department
Knoxville, TN 37996
R. A. Buchanan

UNIVERSITY OF TENNESSEE SPACE INSTITUTE
Tullahoma, TN 37388
J. W. Muehlhauser

WESTERN RESEARCH INSTITUTE
365 N. 9th Street
P.O. Box 3395
University Station
Laramie, WY 82071
V. K. Sethi

WESTINGHOUSE ELECTRIC CORPORATION
Research and Development Center
1310 Beulah Road
Pittsburgh, PA 15235
S. C. Singhal

WESTINGHOUSE HANFORD COMPANY
P.O. Box 1970, W/A-65
Richland, WA 99352
R. N. Johnson

DOE
DOE OAK RIDGE OPERATIONS
P. O. Box 2001
Oak Ridge, TN 37831
Assistant Manager for Energy Research and Development

DOE
DOE OAK RIDGE OPERATIONS
P. O. Box 2008
Building 4500N, MS 6269
Oak Ridge, TN 37831
E. E. Hoffman

DOE
OFFICE OF BASIC ENERGY SCIENCES
Materials Sciences Division
ER-131, GTN
Washington, DC 20545
J. B. Darby

DOE
OFFICE OF FOSSIL ENERGY
Washington, DC 20545
J. P. Carr (FE-72)

DOE
MORGANTOWN ENERGY TECHNOLOGY CENTER
P.O. Box 880
Morgantown, WV 26505
R. A. Bajura
R. C. Bedick
D. C. Cicero
F. W. Crouse, Jr.
N. T. Holcombe
W. J. Huber
J. E. Notestein
J. S. Wilson

DOE
PITTSBURGH ENERGY TECHNOLOGY CENTER
P.O. Box 10940
Pittsburgh, PA 15236
A. L. Baldwin
G. V. McGurl
R. Santore
T. M. Torkos

DOE
OFFICE OF SCIENTIFIC AND TECHNICAL
INFORMATION
P. O. Box 62
Oak Ridge, TN 37831
For distribution by microfiche as shown in DOE/TIC-
4500, Distribution Category:
UC-114 (Coal Based Materials and Components)

DATE
FILMED
6/2/94

END